Effect of metal vaporization behavior on keyhole-mode surface morphology of selective laser melted composites using different protective atmospheres

Donghua Dai [a,b], Dongdong Gu [a,b,*]

[a] College of Materials Science and Technology, Nanjing University of Aeronautics and Astronautics, Yudao Street 29, Nanjing 210016, PR China
[b] Institute of Additive Manufacturing (3D Printing), Nanjing University of Aeronautics and Astronautics, Yudao Street 29, Nanjing 210016, PR China

ABSTRACT

A selective laser melting (SLM) physical model of the change from heat conduction to keyhole-mode process is proposed, providing the transformation of the thermal behavior in the SLM process. Both thermo-capillary force and recoil pressure, which are the major driving forces for the molten flow, are incorporated in the formulation. The effect of the protective atmosphere on the thermal behavior, molten pool dynamics, velocity field of the evaporation material and resultant surface morphology has been investigated. It shows that the motion direction of the evaporation material plays a crucial role in the formation of the terminally solidified surface morphology of the SLM-processed part. For the application of N_2 protective atmosphere, the evaporation material has a tendency to encounter in the frontier of the laser scan direction, resulting in the stack of molten material and the attendant formation of humps in the top surface. As Ar protective atmosphere is used, the vector direction of the evaporation material is typically upwards, leading to a uniform recoil pressure forced on the free surface and the formation of fine and flat melt pool surface. The surface quality and morphology are experimentally acquired, which are in a good agreement with the results predicted by simulation.

© 2015 Elsevier B.V. All rights reserved.

1. Introduction

Recently, the lightweight materials with high strength and stiffness are in an increasing demand and are widely used in the modern industries, such as the aerospace, automotive, microelectronics, etc. [1]. Aluminum matrix composites (AMCs), due to the high strength, outstanding abrasion resistance and low coefficient of thermal expansion, become the promising candidates and have the capacity to meet these crucial demands. The TiC material, due to its high elastic modulus, high hardness and typically its thermodynamic stability within the molten aluminum, is the potentially feasible reinforcement for AMCs [2]. Traditional fabrication methods of AMCs generally require the tooling or dies to manufacture the parts. However, these traditional methods are relatively expensive and at a cost of longer production time, especially for the small production runs of complex shaped parts. Indirect rapid manufacturing

methods typically require the process of green parts followed by the infiltration or the process of a lost wax model followed by the subsequent casting, which are not the true rapid manufacturing technology due to the application of the mould.

Selective laser melting (SLM), as a typically additive manufacturing or 3D printing technology, generally has the capacity to produce an almost unlimited flexibility of complex geometry, allowing rapid manufacturing of the fully-dense and functional parts or tools directly from computer-aided design (CAD) data using various powder materials [3–5]. However, it was found that there exists a processing challenge in the SLM fabrication of AMCs due to the unique physical properties including (i) the considerably low laser energy absorption (only 9%) of the aluminum material, (ii) the high heat conductivity of 237 W/(mK) that is 11-fold compared to Ti material and 5-fold compared to Fe material, (iii) the high affinity to oxygen and elevated oxidation kinetics [2,6]. With the protective gas fed into the processing chamber, the interior oxygen content can be reduced to a rigorous standard, alleviating the formation of oxide films on the surface of the molten pool [7]. The keyhole-mode laser melting additive manufacturing, due to the combined advantages of the multiple reflections of the laser in the vapor cavity and the high efficiency of heat absorption in the powder bed,

* Corresponding author at: College of Materials Science and Technology, Nanjing University of Aeronautics and Astronautics, Yudao Street 29, Nanjing, Jiangsu 210016, China. Tel.: +86 25 52112626; fax: +86 25 52112626.
E-mail address: dongdonggu@nuaa.edu.cn (D. Gu).

Nomenclature

B	View factor
C_p	Specific heat at constant pressure, J/(kg K)
D_p	Average diameter of the powder particles, m
E	Energy, J
F	Body force, e.g. gravity and buoyancy forces, N
g	Gravity, m/s^2
h, h_s	Enthalpy
h_c	Convective heat-transfer coefficient, W/(m^2 K)
h_{ref}	Reference enthalpy
H	Enthalpy of the material
ΔH	Latent heat of the phase change
ΔH_{LV}	Latent heat of evaporation
I	Turbulent intensity
M_s	Mass source, kg
$\dot{M}_{\xi\zeta}, \dot{M}_{\zeta\xi}$	mass transfer from phase ξ (ζ) to phase ζ (ξ)
N	Normal component
p, p_0	Pressure, N/m^2
P	Laser power, W
q_v	Heat losses due to evaporation, J
R	Gas constant
R'	Radius of the surface curvature
S_H	Source item of the energy conservation
S_{α_ξ}	Mass source for each phase
t	Time, s
T_b, T_{LV}, T_m	Temperature, K
T_∞	Ambient temperature, K
T_p	Temperature of the powder particles, K
$\vec{V}, V$	Velocity vector, m/s
u, v, w	Velocity magnitude, m/s
x, y, z	Coordinates, m
$\alpha, \alpha_i, \alpha_\xi$	Volume fraction
α_p	Fraction of particles
β	Drag coefficient
γ	Surface tension, kg/m
ε	Radiation emissivity
κ	Thermal conductivity of the powder bed, W/(m K)
κ_{eff}	Effective thermal conductivity of liquid–solid–gas multi-phases, W/(m K)
κ_f	Thermal conductivity of the fluid, W/(m K)
κ_r	Thermal conductivity due to the radiation among particles, W/(m K)
κ_s	Thermal conductivity of the solid, W/(m K)
μ	Dynamic viscosity, Pa s
ρ, ρ_i, ρ_ξ	Coupled density, kg/m^3
σ_e	Stefan–Boltzmann constant

a SLM-processed part are significantly critical in many industry applications, requiring a fine surface to avoid premature failure from surface initiated cracking [10]. It seems that little work has been paid attention to the effect of the protective atmosphere on the surface morphology of the SLM-processed parts. More recently, the effect of the protective atmosphere on the structure and properties of SLM-processed Al alloy was studied by Sercombe and co-workers [11]. It was concluded that the density obtained in the SLM-processed part was not significantly influenced using different atmosphere types (Ar, N$_2$ and He) and, clusters of pores were apparently appeared as He protective atmosphere was used. For the keyhole-mode SLM processing of AMCs, it seems that the combined influence of the protective atmosphere types and the evaporation material on the metallurgical behavior of the molten pool and the resultant surface morphology has not been studied in detail.

In this paper, the numerical simulation regarding the protective atmosphere on the thermodynamics of the molten pool and resultant variation of the top surface finish during SLM of TiC/AlSi10Mg composite materials was carried out, using Fluent 6.3.26 commercial finite volume method (FVM) software. The fluid flow driven by the combined effect of the surface tension gradient and recoil pressure caused by the evaporation material is considered in the physical model and the temperature distribution, the change of the heat transfer method, keyhole evolution, velocity field of the evaporation material and the resultant top surface morphology were simulated. Furthermore, the top surface morphologies of the SLM-processed parts obtained by numerical simulation were compared with those acquired via experiments, in order to testify the accuracy of the established simulation model and have a thorough understanding of the influence of the protective atmosphere on the top surface morphology.

2. Model descriptions

Fluent 6.3.26 software, which enables the simulation of the thermal behavior, melting-solidification process, velocity field and the metal evaporation phenomenon, is introduced to simulate SLM of the TiC/AlSi10Mg powder process in this paper. In order to simplify the problem involved in the SLM process, the following assumptions are made in this study [12]: (1) The melt in the molten pool is assumed to be incompressible homogeneous Newtonian fluid; (2) Except thermal conductivity, surface tension, viscosity and specific heat, some other thermal physical constants are considered to be temperature independent.

2.1. Physical model

The schematic of the SLM physical phenomena is generally depicted in Fig. 1a. Laser beam is typically treated as a volume heat source and it is defined as a Gaussian function. The solid phase (TiC/AlSi10Mg powder material) is defined with the three dimensions of 30 μm × 30 μm × 30 μm in the present physical model, having a close estimation with the volume of the powder material used in the SLM process [13]. The free surface fluctuation of the molten pool is significantly determined by the combined effect of the surface tension and the recoil pressure caused by the material evaporation. Therefore, an interface between the solid phase and the protective atmosphere is accordingly established, taking account of the heat, mass and momentum transfer in the melting-phase change-solidification process. The initially physical condition of the mathematical model is shown in Fig. 1b. The three dimensions of the physical model are set with the value of 6 mm × 3 mm × 1 mm. The protective atmosphere is defined and

was proposed and analyzed mathematically [8]. The keyhole-mode laser melting enables the laser energy transfer to a far deeper distance in the AMCs powder layer, improving the utilization rate of the laser energy and enhancing the SLM processability of AMCs parts. It seems that the keyhole-mode laser melting provides an alternative method to solve the challenge of SLM fabrication of AMCs due to the aforementioned physical properties.

SLM is a complex physical metallurgical process involving multi-modes of mass, heat and momentum transfer and significantly depends on the processing parameters (typically including scan speed, laser power, scan spacing, layer thickness and scan strategy) [9]. Therefore, considerable efforts have been expended on the previous researches, focused on the various materials to optimize the processing parameters with the aim of improving microstructure, density, surface quality/roughness and the attendant mechanical properties. Both of the density and surface morphology of

initiated in the laser penetration direction ($Z = 0.6$–1 mm) and thus the other region ($Z = 0$–0.6 mm) is the solid phase consisting of the TiC and AlSi10Mg material with the volume ratio of 1:9 in the physical model. The physical properties of the molten pool under various protective atmospheres (N_2, Ar and He) are cited [14]. In order to have a better investigation of the thermal behavior transferring from heat conduction to keyhole-mode SLM process, the temperature fields are extracted at the iteration time of 6×10^{-4} s, 3×10^{-3} s, 5.4×10^{-3} s and 6×10^{-3} s, respectively. The real time SLM process and the laser source are depicted in Fig. 1c and d, respectively.

2.2. Governing equations

The governing equations for mass, momentum and energy conversations are summarized as follows [15]:

2.2.1. Mass conservation

$$\frac{\partial \rho}{\partial t} + \nabla \left(\rho \vec{V} \right) = M_s \tag{1}$$

2.2.2. Momentum conservation

$$\rho \left(\frac{\partial \vec{V}}{\partial t} + \vec{V} \cdot \nabla \vec{V} \right) = \mu \nabla^2 \vec{V} - \nabla p + M_s \cdot \vec{V} + F \tag{2}$$

2.2.3. Energy conservation

$$\frac{\partial(\rho T)}{\partial t} + \frac{\partial(\rho u T)}{\partial x} + \frac{\partial(\rho v T)}{\partial y} + \frac{\partial(\rho w T)}{\partial z} = \frac{\partial}{\partial x}\left(\kappa \frac{\partial T}{\partial x} \right) + \frac{\partial}{\partial y}\left(\kappa \frac{\partial T}{\partial y} \right)$$
$$+ \frac{\partial}{\partial z}\left(\kappa \frac{\partial T}{\partial z} \right) + S_H \tag{3}$$

where $\vec{V}$ is the molten metal velocity. ρ the density, κ the thermal conductivity, μ the viscosity, p the pressure and M_s is the mass source, including the particle mass. S_H is the source item of the energy conservation and can be expressed as:

$$S_H = - \left(\frac{\partial}{\partial t}(\rho \Delta H) + \nabla \cdot \left(\rho \vec{V} \Delta H \right) \right) \tag{4}$$

where ΔH is the latent heat of phase change. The enthalpy of the material is computed as the sum of the sensible enthalpy, h, and the latent heat, ΔH. The enthalpy of the material, H, can be defined by:

$$H = h + \Delta H \tag{5}$$

where $h = h_{ref} + \int_{T_{ref}}^{T} C_p dT$.

2.3. Keyhole threshold

The threshold for the keyhole-mode melting is determined by the normalized enthalpy, combing the effect of the laser power, scan speed and the radius of the laser beam. According to Hahn and co-workers, an estimate for the criteria of the keyhole-mode threshold in terms of the normalized enthalpy is as follows [16]:

$$\frac{\Delta H}{h_s} = \frac{\pi T_b}{T_m} \tag{6}$$

where h_s is the enthalpy at melting, T_m the melting temperature and T_b is the material boiling temperature.

2.4. Recoil pressure

Generally, a recoil momentum produced by the vaporized material exerts a force on the molten material as the operating temperature is high enough. It can be summarized as follows [17]:

$$-p + 2\mu \frac{\partial V_N}{N} = -0.54 p_0 \exp\left(\Delta H_{LV} \frac{T - T_{LV}}{RTT_{LV}} \right) + \frac{\gamma}{R'} \tag{7}$$

where γ is the surface tension coefficient, R' the radius of the surface curvature, N the normal component, ΔH_{LV} the latent heat of evaporation and p_0 is the argon protective atmosphere. T is the surface temperature, T_{LV} the liquid–vapour equilibrium temperature and R the universal gas constant.

2.5. Marangoni flow

The Marangoni flow caused by the temperature gradient under different protective atmospheres can be described as [18]:

$$-\mu \frac{\partial u}{\partial z} = \frac{\partial \gamma}{\partial T} \frac{\partial T}{\partial x} \tag{8}$$

$$-\mu \frac{\partial v}{\partial z} = \frac{\partial \gamma}{\partial T} \frac{\partial T}{\partial y} \tag{9}$$

2.6. Equations of volume of fluid (VOF) model

The volume fraction equation for the i phase is [19]:

$$\frac{\partial \alpha_i}{\partial t} + \vec{V} \cdot \nabla \alpha_i = \frac{S_{\alpha_i}}{\rho_i} \tag{10}$$

where $\sum_{i=1}^{n} \alpha_i = 1$, n represents the phase number.

The resulting velocity field is shared among the phases [19]:

$$\frac{\partial}{\partial t}\left(\rho \vec{V} \right) + \nabla \left(\rho \vec{V} \right) = -\nabla p + \nabla \left[\mu \left(\nabla \vec{V} + \nabla \vec{V}^T \right) \right] + \rho g + \vec{F} \tag{11}$$

Both of the density ρ and dynamic viscosity μ in Eq. (11) depends on the volume fraction of all phases:

$$\rho = \sum \alpha_i \rho_i \tag{12}$$

$$\mu = \sum \alpha_i \mu_i \tag{13}$$

The energy equation shared among the phases is defined by [19]:

$$\frac{\partial}{\partial t}(\rho E) + \nabla \left[\vec{V}(\rho E) + \rho \right] = \nabla(\kappa_{eff} \nabla T) + S_h \tag{14}$$

In this model, the energy, E, and temperature, T, are treated as mass-averaged variables:

$$E = \frac{\sum_{i=1}^{n} \alpha_i \rho_i E_i}{\sum_{i=1}^{n} \alpha_i \rho_i} \tag{15}$$

where E_i is generally based on the specific heat of that phase and the shared temperature. κ_{eff} is the effective thermal conductivity and also shared by the phases. S_H is the source term and contains radiation as well as any other volumetric heat sources.

The tracking of the interface(s) between the various phases is defined by the solution of a continuity equation. For the ξ phase [20]:

$$\frac{1}{\rho_\xi}\left[\frac{\partial}{\partial t}\left(\alpha_\xi \rho_\xi \right) + \nabla \left(\alpha_\xi \rho_\xi \vec{V}_\xi \right) \right] = S_{\alpha_\xi} + \sum_{\zeta=1}^{n} \left(\dot{M}_{\xi\zeta} - \dot{M}_{\zeta\xi} \right) \tag{16}$$
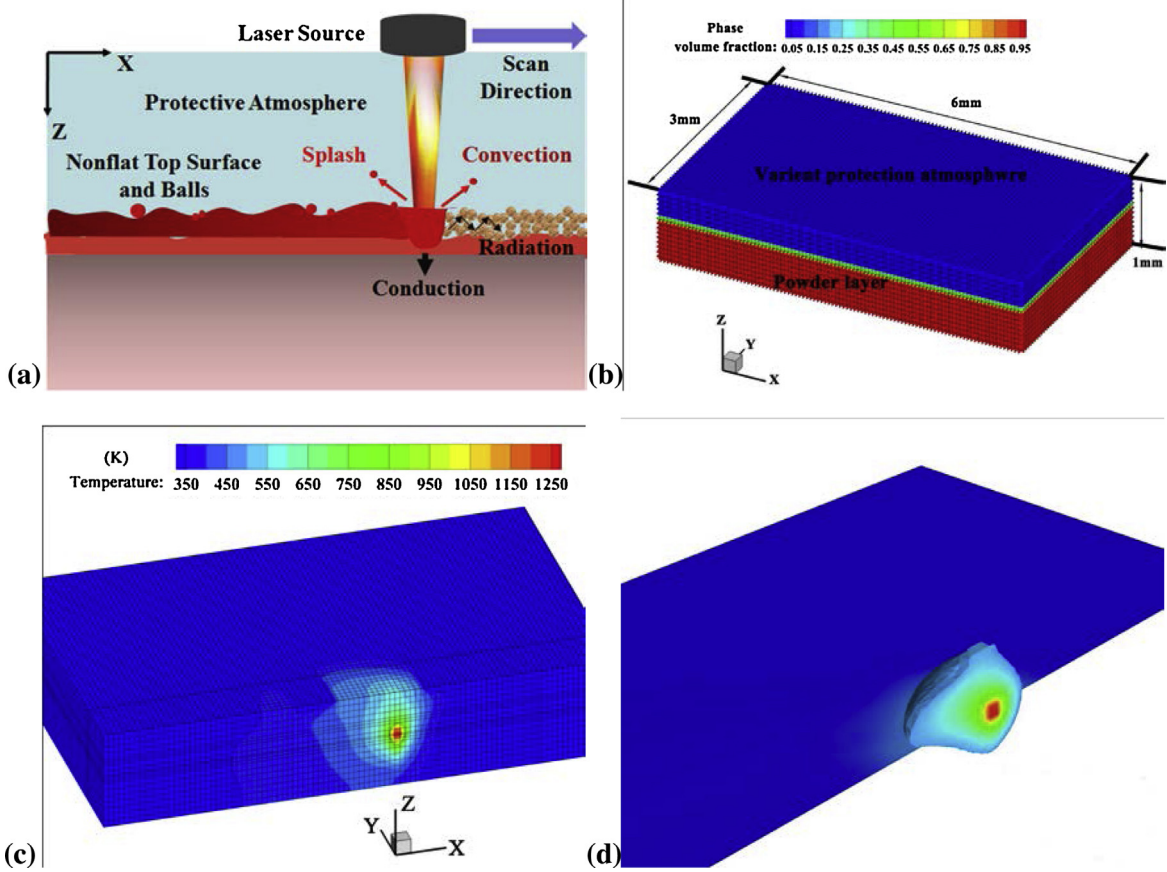
Fig. 1. Schematic of the SLM physical model (a), the initial stage of the established mathematical model (b), the SLM processing procedure (c) and the laser heat source used in SLM process (d).

where $\dot{M}_{\xi\zeta}$ ($\dot{M}_{\zeta\xi}$) is the mass transfer from phase $\boldsymbol{\xi}$ ($\boldsymbol{\zeta}$) to phase $\boldsymbol{\zeta}$ ($\boldsymbol{\xi}$). S_{α_ξ} is the user-defined mass source.

2.7. Thermal boundary conditions

The energy fluxes, combined with the heating by the absorbed energy from the laser beam and the cooling by protective atmosphere convection, thermal radiation and material evaporation, are defined in the interface between the protective atmosphere and solid phase [13].

$$-\kappa\left(\frac{\partial T}{\partial t}\right)_{z=0.0006} = q|_{z=0.0006} - h_c(T - T_\infty) - \sigma_e\varepsilon(T^4 - T_\infty^4) - q_v$$

(17)

Table 1
As-used material properties and SLM processing conditions.

Parameter	Value
Ambient temperature, T_∞	300 K
Convective heat-transfer coefficient, h_c	80 W/(m² K)
The Stefan–Boltzmann constant, σ	5.67×10^{-8} W/(m² K⁴)
Radiation emissivity, ε	0.36
Powder layer thickness, l_p	50 μm
Laser power, P	160 W
Scan speed, V	300 mm/s
Radius of laser beam, ω	35 μm
Melting and evaporation point of TiC	3430 K, 5090 K
Melting and evaporation point of AlSi10Mg	893 K, 2743 K
Melting latent	5.03×10^5 J/kg
Evaporation latent	1.07×10^7 J/kg

where q is the heat flux due to multiple reflection Fresnel absorption, which is studied by the researcher [12], h_c the heat transfer coefficient of natural thermal convection, T_∞ the ambient temperature, σ_e the Stefan–Boltzmann constant and ε is the emissivity. q_v denotes the heat losses due to the evaporation.

2.8. Physical properties

The effective thermal conductivity of the powder bed, κ, is estimated [21]:

$$\frac{\kappa}{\kappa_f} = \left(1 - \sqrt{1-\alpha}\right)\left(1 + \frac{\alpha\kappa_r}{\kappa_f}\right)$$
$$+ \sqrt{1-\alpha}\left[\frac{2}{1-\frac{\kappa_f}{\kappa_s}}\left(\frac{1}{1-\frac{\kappa_f}{\kappa_s}}\ln\left(\frac{\kappa_s}{\kappa_f}\right) - 1\right) + \frac{\kappa_r}{\kappa_f}\right]$$

(18)

where α is the fractional porosity in the powder bed, κ_f and κ_s are the thermal conductivity of the melt and the thermal conductivity of the solid, respectively. κ_r is the thermal conductivity caused by the radiation in the powder bed, which is further defined:

$$\kappa_r = 4B\sigma_e T_p^3 D_p$$

(19)

where D_p and T_p are the average diameter and temperature of the powder particles, respectively. σ_e is the Stefan–Boltzmann constant, B is a view factor and approximately taken as 1/3.

2.9. Numerical simulation

The simulation is carried out using the FLUENT commercial finite volume method package (version 6.3.26) to simulate the thermal
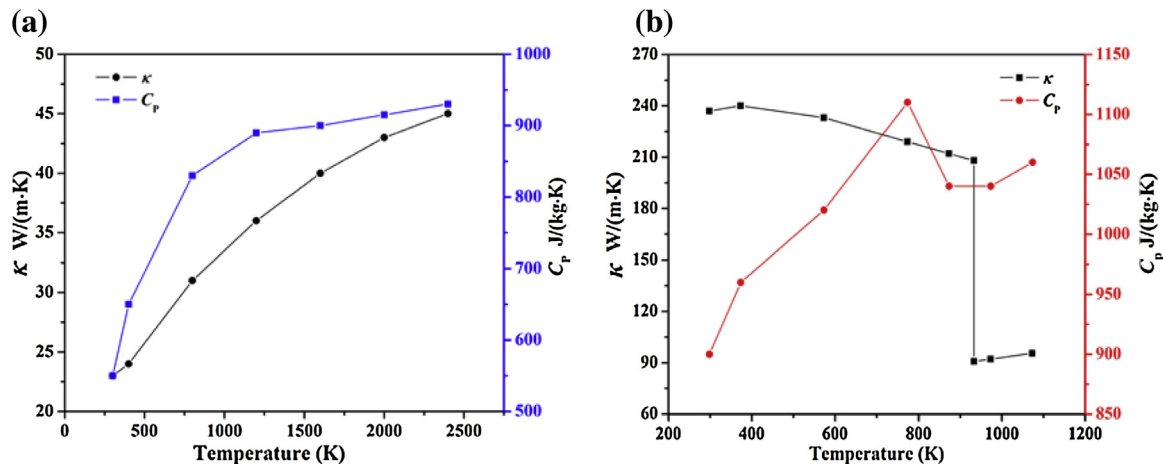
Fig. 2. Thermal conductivity and specific heat capacity of as-used materials: (a) TiC; (b) AlSi10Mg.

behavior, velocity field of the evaporation material, keyhole depth fluctuation and the resultant top surface morphology. The thermal physical properties of AlSi10Mg and TiC materials are depicted in Fig. 2 [22,23]. The SLM processing parameters depending on our previous research ($P = 160$ W, $V = 300$ mm/s) are chosen and shown in Table 1.

3. Experimental procedures

3.1. Powder materials

The 99.0% purity TiC nanopowder with an average particle size of 50 nm and the 99.7% purity and spherically shaped AlSi10Mg powder with a mean particle diameter of 30 μm were used. The TiC/AlSi10Mg composite powder system with a near spherical shape and a homogeneous particle size distribution is experimentally obtained using the ball milling process. It is obvious that the nanoscaled TiC particles are homogeneously distributed around the AlSi10Mg particle surface, leading to a good flowability and homogeneous physical properties [13].

3.2. Processing and characterization

The SLM system consisted mainly of a IPG YLR-200-SM ytterbium fiber laser with a power of ∼200 W and a spot size of 70 μm, a SCANLAB hurrySCAN® 20 scanner, an automatic powder spreading system, an inert protective atmosphere system, and a computer system for process control. The processing conditions investigated are the same as the data in the numerical simulation. Specimens for metallographic examinations were ground and polished according to the standard procedures. The low-magnification of the SLM-processed specimens was observed using a PMG3 optical microscope (OM) (Olympus Corporation, Japan). The typical top surface morphology study of the SLM-processed parts was characterized using a Hitachi S-4800 field emission SEM (FE-SEM) at 5 kV.

4. Results and discussion

4.1. Energy transfer mechanisms

SLM process can be classified as either thermal conduction or keyhole-mode laser processing. Fig. 3 shows the typical temperature field variation under different iteration time 6×10^{-4} s,

3×10^{-3} s, 5.4×10^{-3} s and 6×10^{-3} s. The temperature field is typically Gauss function due to the definition of the Gaussian heat source (Fig. 3 and Fig. 1d). It is evident that the molten pool depth, namely laser penetration ability, gradually increases and reaches a comparable fixed depth and then fluctuates as the SLM process proceeds. From the start of the calculation process at $t = 6 \times 10^{-4}$ s, the shallow molten pool profile is approximately conical and the highest temperature is obtained in the center part of the molten pool (Fig. 3a), approaching the boiling temperature of the powder material (Table 1). The free surface of the molten pool is significantly covered by the higher temperature gas of the evaporation metal (Fig. 3a). Therefore, a recoil pressure is accordingly produced, leading to the motion and the attendant deformation of the free surface. At the iteration time $t = 3 \times 10^{-3}$ s, the keyhole molten pool has a tendency to become stable combined with the evaporation metal near the laser beam irradiation area (Fig. 3b). As the SLM process further proceeds at $t = 5.4 \times 10^{-3}$ s, a stable and collapse free keyhole is successfully produced in the longitudinal section of the molten pool (Fig. 3c). Moreover, the evaporation metal gas is entirely covered near the keyhole center from the transient temperature field, thus leading to the occurrence of strong ablation and the resultant recoil pressure forced on the molten pool [24]. At the iteration time $t = 6 \times 10^{-3}$ s, the keyhole is completely the same as that obtained at $t = 5.4 \times 10^{-3}$ s, indicating that a stable and desired keyhole is reasonably obtained after 5.4 ms (Fig. 3d). From the start of the SLM process, it seems that the evaporation metal gas is fulfilled in the processing chamber rather than near the center of the molten pool (Fig. 3a). This phenomenon can be analyzed that the absorbed energy is preferentially used to heat and melt the metal powder in the upper region of the powder layer and subsequently overcome the melting and evaporation latent heat barrier of the material [24]. In this processing condition, the molten pool depth is considerably controlled by the conduction of heat in the underlying solid material. As the SLM process proceeds, the latent heat barrier of the material is accordingly overcome due to the heat effect of the laser beam. Therefore, the operating temperature obtained in the molten pool is significantly higher than the boiling temperature, producing strong evaporation phenomena and resultantly enhancing the keyhole depth to an approximate depth (Fig. 3c and d). The depth of the molten pool is controlled by the evaporation metal and the attendant recoil pressure. Therefore, the mechanism of the melting process typically changes from heat conduction to the keyhole-mode processing. It is confirmed that the molten pool depth obtained in the keyhole-mode processing is much deeper than that in the heat conduction.
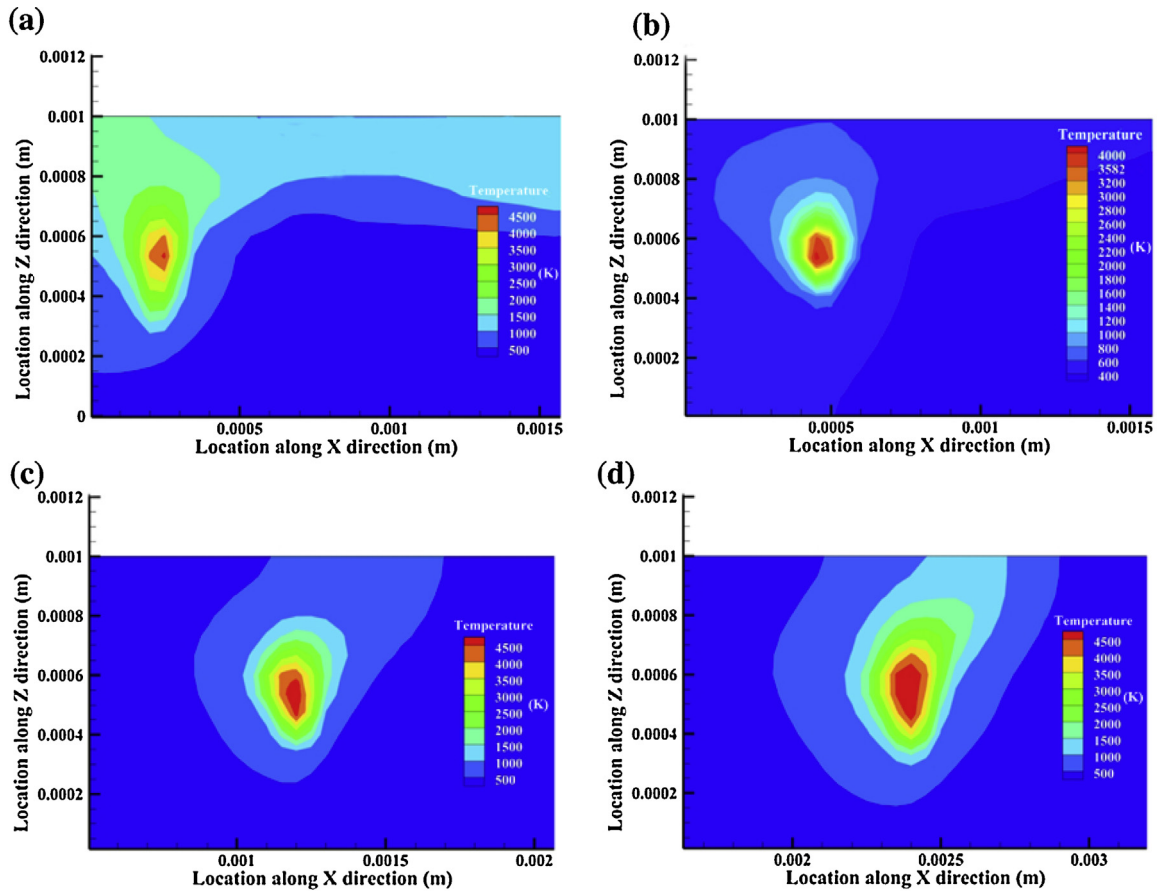
Fig. 3. Typical temperature field variation under different iteration times: 6×10^{-4} s (a), 3×10^{-3} s (b), 5.4×10^{-3} s (c) and 6×10^{-3} s (d).

4.2. Keyhole depth variation

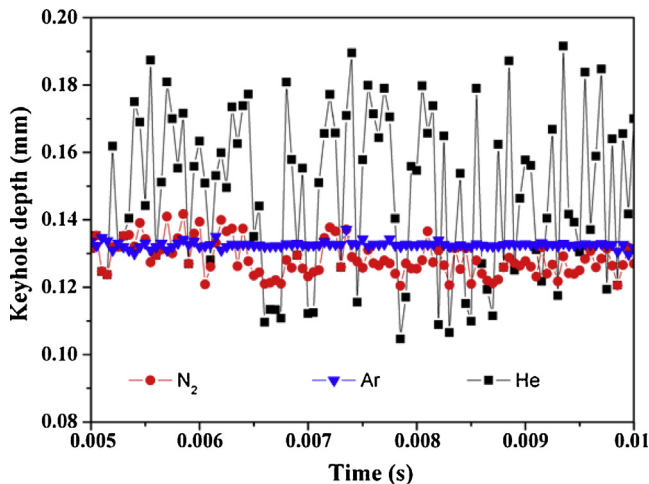Fig. 4 shows the typical molten pool depth variation curves during keyhole-mode SLM process using different protective atmospheres (at iteration time $t = 5$–10 ms). The maximum distance measured from the top surface of the molten pool to the point of the keyhole wall along the penetration direction is defined as the keyhole depth. It is evident that the keyhole depth fluctuates around a certain value using different protective atmospheres. As He protective atmosphere is used, there is a serious fluctuation of the keyhole depth with the maximum and minimum value of 190 μm and 110 μm, respectively. Generally, it indicates that an unstable keyhole is caused by the serious depth fluctuation in SLM process, having a tendency to produce the residual pores in the solidified part due to the occurrence of the keyhole collapse. As N_2 protective atmosphere is employed, a slight molten pool fluctuation is obviously observed with the variation range of 20 μm. However, as Ar protective atmosphere is used, the keyhole depth during iteration time from 5 ms to 10 ms exhibits a relatively stable behavior with the average value of 132 μm. It has been found that a small depth fluctuation typically refers to the stable state and collapse free of the molten pool and, thus few or none bubbles are trapped in the molten pool [22]. As a result, for the keyhole-mode SLM process, it seems that Ar protective atmosphere has the stabilization ability to significantly decrease the keyhole molten pool fluctuation and, therefore a dense SLM-processed part will be obtained. It is remarked that this simulation result has a similar trend with experimental work conducted by Wang and Sercombe [23]. It can be reasonably concluded that the present mathematical model has the capacity to predict the residual porosity defect induced by the molten pool instability in the keyhole-mode SLM process.

4.3. Morphologies of the top surface

Typical surface morphologies of the SLM-processed part predicated by the keyhole-mode simulation method using different protective atmospheres are depicted in Fig. 5. It is obvious that the protective atmosphere plays a key role in the formation of the top surface morphology in the SLM-processed part. For the application of He protective atmosphere, the serious surface morphology curvatures combined with some residual pores are obviously appeared
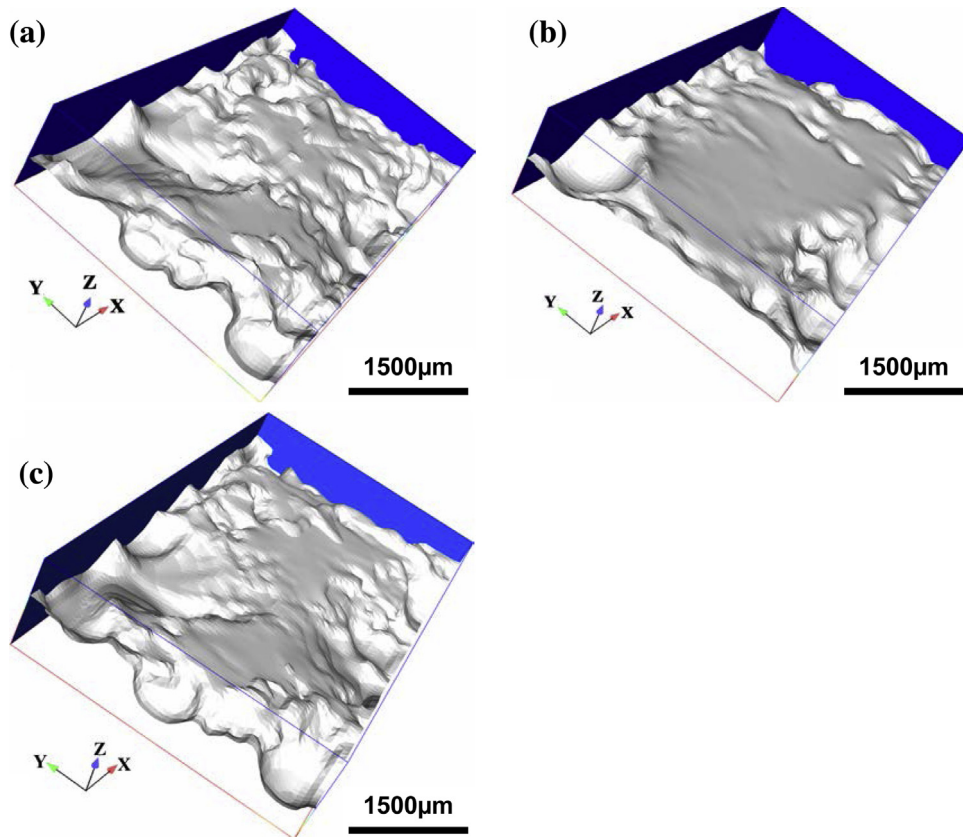

Fig. 4. Typical molten pool depth variation curves during keyhole-mode SLM process using different protective atmospheres.

Fig. 5. Surface morphologies of the keyhole-mode SLM-processed part predicated by the simulation method using different protective atmospheres: (a) He, (b) Ar and (c) N_2.
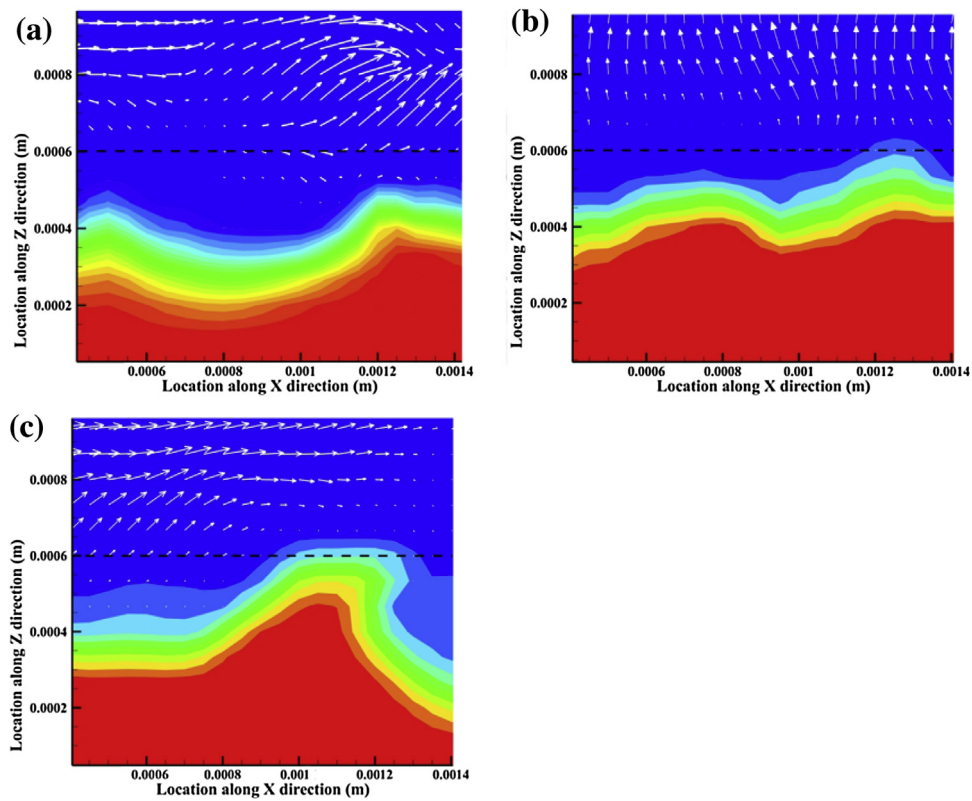

Fig. 6. Velocity field of the vaporization material and the volume fraction contours: (a) He, (b) Ar and (c) N_2.
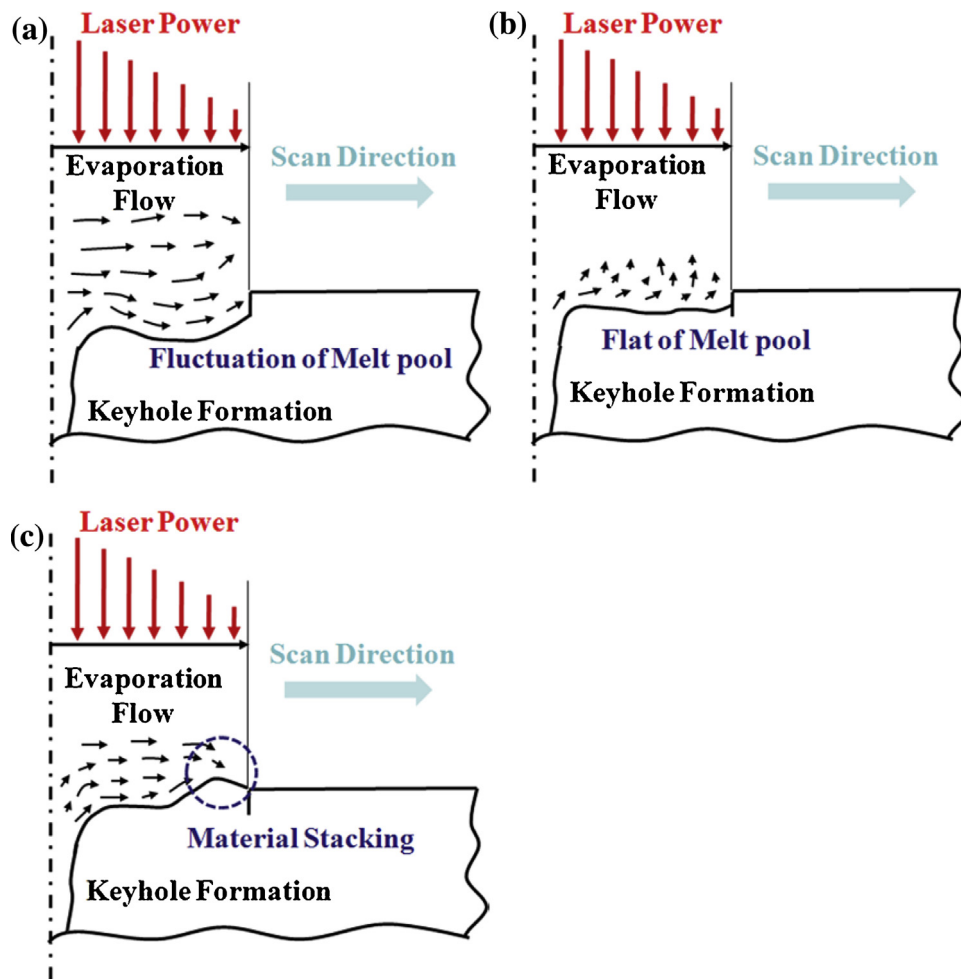
Fig. 7. Effect of the vaporization metal velocity field on the top surface morphology is depicted: (a) He, (b) Ar and (c) N_2.

in the solidified part, resulting in the formation of the poor surface quality and the attendant response of the low densification (Fig. 5a). As Ar protective atmosphere is used, the relatively smooth and completely dense surface morphology is produced, showing no serious fluctuation and few apparent pores (Fig. 5b). For the application of N_2 protective atmosphere, it is obvious that a material stacking is typically produced, resulting in the formation of the humps in the free surface and a slight reduction in the relative densification. As a result, the surface quality has a tendency to become worse compared with that obtained at the application of Ar protective atmosphere (Fig. 5c).

In order to investigate the influence of the protective atmosphere on the surface morphology of the molten pool, the velocity field of the evaporation material and the volume fraction contours are shown in Fig. 6. It is worth noting that the velocity field of the evaporation material is significantly sensitive to the application of the protective atmosphere. For the application of He protective atmosphere, an apparent concave profile located in the top surface of the molten pool is produced with the maximum and minimum height value of 0.00055 m and 0.0003 m in the laser penetration direction, respectively (Fig. 6a), implying a considerable fluctuation of the molten pool. The main velocity field vector of the evaporation metal is in the combination of horizontal direction and downward direction, giving rise to the formation of the concave in the molten pool (Fig. 6a). As Ar protective atmosphere is applied, a relatively steady-state behavior in the top surface of the molten pool is generally obtained and, the average height of the molten pool is fluctuated around 0.0005 m, implying the occurrence of the

slight disturbance of the molten pool (Fig. 6b). Meanwhile, it is clear that the vector of the velocity field in the top surface is absolutely upward. Therefore, the recoil pressure caused by the evaporation metal is uniformly forced on the free surface of the molten pool, leading to the achievement of the local disturbance and flat top surface (Fig. 6b). For the application of N_2 protective atmosphere, it is obvious that a material stacking is apparently located in the frontier of the molten pool region with the maximum and minimum height 0.0006 m and 0.0003 m, respectively (Fig. 6c). The vector of the velocity field from the evaporation metal has a tendency to encounter in the laser beam scan direction, resulting in the formation of the material stacking. As a result, it is reasonable to conclude that a limited and poor surface morphology is produced in this application of the protective atmosphere.

The effect of the evaporation metal velocity field on the top surface morphology is depicted in Fig. 7. For the application of He protective atmosphere, a serious fluctuation in the molten pool depth and the attendant keyhole collapse is apparently generated, caused by the instability of the keyhole-mode SLM process (Fig. 4). Meanwhile, the main vector of the evaporation metal is generally in the combination of horizontal direction and downward direction, resulting in the formation of non-uniform recoil pressure forced on the free surface of the molten pool (Fig. 6a). Therefore, a poor surface morphology with residual pores in the solidified part is subsequently produced (Fig. 5a and 6a), caused by the occurrence of the concave profile in the free surface of the molten pool. As Ar protective atmosphere is used, a combination of the stable state and the collapse free of the molten pool is generally
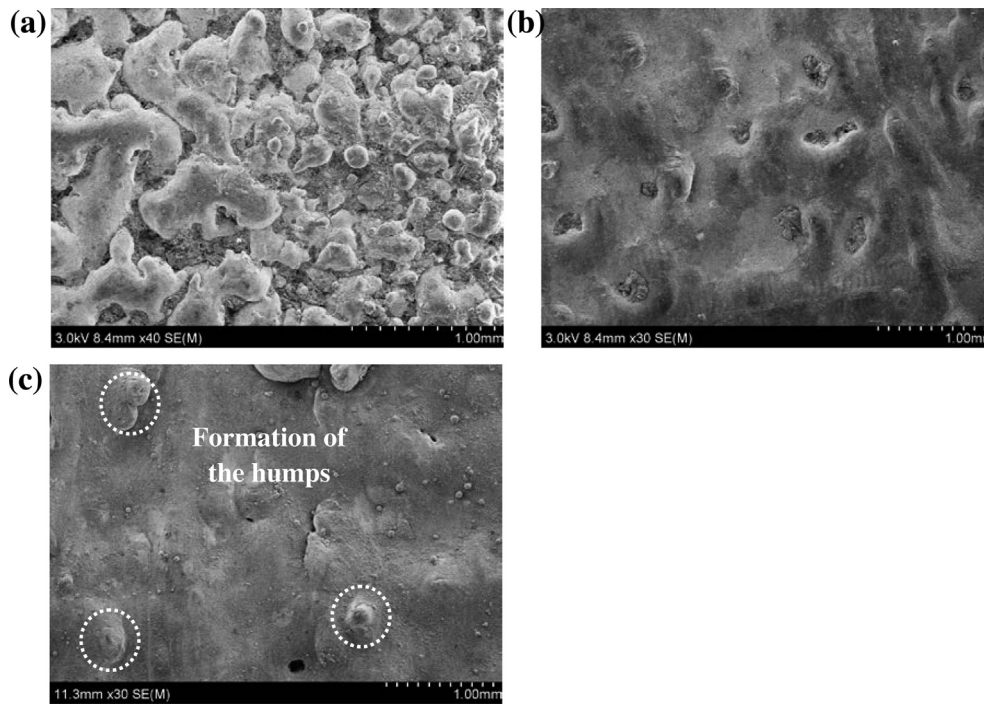
Fig. 8. Surface morphologies obtained in the SLM processed TiC/AlSi10Mg parts using various protective atmospheres: (a) He, (b) Ar and (c) N₂.

formed, leading to the formation of few or none bubbles entrapped in the molten pool (Fig. 4). The vector of the evaporation metal is completely upward direction (Fig. 6b), reasonably producing a uniform recoil pressure forced on the free surface of the molten pool and as a result, a relatively flat surface morphology combined with a dense metallurgical bonding ability is obtained in the SLM-processed part (Fig. 5b and Fig. 7b). For the application of N₂ protective atmosphere, a slight fluctuation in the depth of the molten pool is produced compared with that obtained in Ar protective atmosphere (Fig. 4). The vector of the velocity field from the evaporation metal has a tendency to encounter in the

frontier of the laser beam-powder interaction region, resulting in the formation of the material stacking and decreasing the surface quality of the solidified part (Fig. 5c and Fig. 7c). Meanwhile, a decreased response of the relative density in the SLM-processed part is formed due to the non-uniform spreading of the material.

4.4. Experimental verification

The typical surface morphologies obtained in the SLM processed TiC/AlSi10Mg parts using various protective atmospheres are depicted in Fig. 8. For the application of He protective atmosphere,
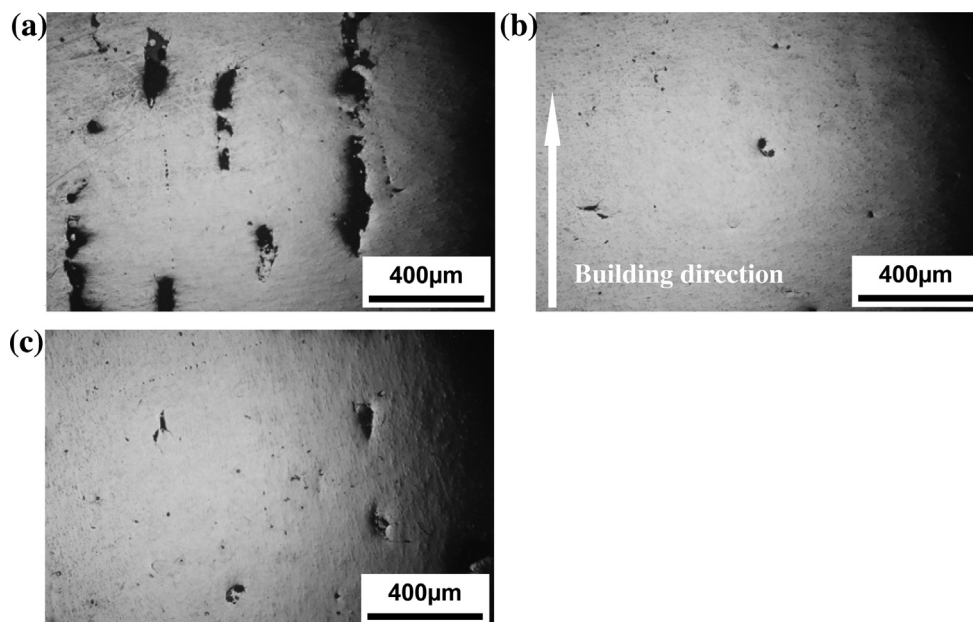

Fig. 9. Optical microscopy images showing interlayer microstructures on cross-sections along the laser scan direction of SLM-processed TiC/AlSi10Mg parts using various protective atmospheres: (a) He, (b) Ar and (c) N₂.
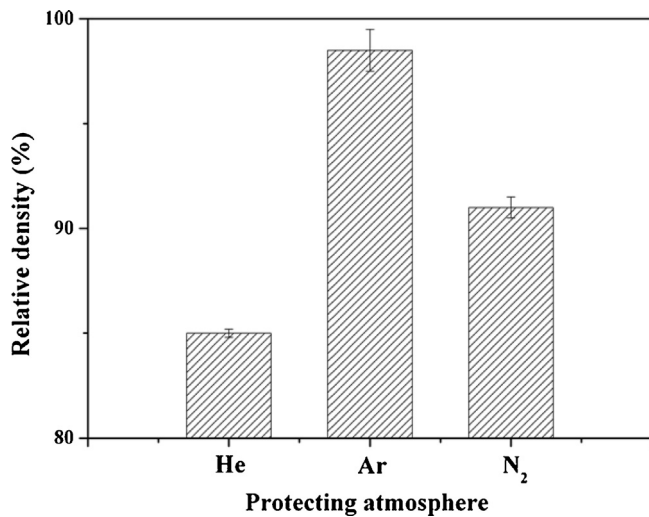
Fig. 10. Relative density obtained in the SLM-processed part using different protective atmospheres.

a poor surface morphology in the combination of the discontinuous scan tracks was produced due to the formation of serious fluctuation and instability of the molten pool (Fig. 8a). As Ar protective atmosphere was used, a fine surface morphology of the SLM-processed TiC/AlSi10Mg with perfect inter-track bonding was successfully produced, showing no obvious pores and cracks (Fig. 8b). For the application of N_2 protective atmosphere, a serious material stacking phenomenon was apparently produced on the surface of the SLM-processed part due to the encounter of the evaporation metal, resulting in the formation of humps and the limited surface quality (Fig. 8c). Meanwhile, it was obvious that a few pores were present on the surface of the solidified part, reducing the densification response and restricting the application of the produced part.

Fig. 9 shows the cross-sections of the SLM-processed TiC/AlSi10Mg parts using various protective atmospheres. For the application of He protective atmosphere, a large amount of large-sized residual pores, along the building direction, was produced in the solidified part with the average length of 200 μm (Fig. 9a), caused by the fluctuation of the molten pool and the keyhole collapse (Fig. 4). Therefore, in this processing condition, the insufficient densification response was only 85% (Fig. 10). As Ar protective atmosphere was used, a denser part free of residual pores was obtained and the obtained densification level increased to 98.5% (Fig. 10), due to the formation of the stable-state molten pool (Fig. 4). For the application of N_2 protective atmosphere, a small amount of remained pores were remained in the SLM-processed part, slightly decreasing the densification level to 91% owing to formation of the material stacking and resultant formation of humps. Therefore, a close look at the experiment and simulation results reveals that the surface morphology and residual pores predicted by the physical model established in this paper are in a good agreement with the simulation results.

5. Conclusions

The simulation of the molten pool dynamics changing from the heat conduction to the keyhole-mode SLM process and the top surface quality of SLM-processed TiC/AlSi10Mg parts has been carried out, using a finite volume method (FVM) and the following conclusions can be drawn.

(1) The molten pool depth, namely laser penetration ability, gradually increases and reaches a comparable fixed depth and then fluctuates as the SLM process proceeds. The depth of the molten pool is controlled by the conduction of heat and the resultant recoil pressure caused by the evaporation of the metal as the SLM process proceeds.

(2) There is a significant difference in the fluctuation behavior of the molten pool using different protective atmospheres. It seems that Ar protective atmosphere has the stabilization ability to significantly decrease the keyhole molten pool fluctuation and, therefore a dense SLM-processed part will be obtained.

(3) The applied protective atmosphere plays a crucial role in determining the surface quality of the SLM-processed part. For the application of Ar protective atmosphere, a stable-state of the molten pool depth combined with a uniform recoil pressure forced on the free surface of the molten pool is typically produced, leading to the formation of a sound surface morphology.

(4) The surface quality and relative density are experimentally obtained and have a good accordance with the results predicted by the simulation. The physical issues considered in the mathematical model are completely general. Therefore, the SLM physical model established in this paper is completely suitable for other powder system.

References

[1] S. Sharifi Golru, M.M. Attar, B. Ramezanzadeh, Appl. Surf. Sci. 345 (2015) 360–368.
[2] D.D. Gu, Laser Additive Manufacturing of High-Performance Materials, Springer-Verlag, Berlin, Heidelberg, 2015, ISBN 978-3-662-46088-7.
[3] B.C. Zhang, H.L. Liao, C. Coddet, Appl. Surf. Sci. 279 (2013) 310–316.
[4] R.D. Li, Y.S. Shi, Z.G. Wang, L. Wang, J.H. Liu, W. Jiang, Appl. Surf. Sci. 256 (2010) 4350–4356.
[5] A.V. Gusarov, I. Yadroitsev, Ph. Bertrand, I. Smurov, Appl. Surf. Sci. 254 (2007) 975–979.
[6] E. Louvis, P. Fox, C.J. Sutcliffe, J. Mater. Process. Technol. 211 (2011) 275–284.
[7] B.C. Zhang, L. Zhu, H.L. Liao, C. Coddet, Appl. Surf. Sci. 263 (2012) 777–782.
[8] A.F.H. Kaplan, Appl. Surf. Sci. 258 (2012) 3354–3363.
[9] D.D. Gu, W. Meiners, K. Wissenbach, R. Poprawe, Int. Mater. Rev. 57 (2012) 133–164.
[10] W. Zhu, L. Yang, J.W. Guo, Y.C. Zhou, C. Lu, Appl. Surf. Sci. 315 (2014) 292–298.
[11] X.J. Wang, L.C. Zhang, M.H. Fang, T.B. Sercombe, Mater. Sci. Eng. A 597 (2014) 370–375.
[12] S.C. Li, G.Y. Chen, S. Katayama, Y. Zhang, Appl. Surf. Sci. 303 (2014) 481–488.
[13] D.H. Dai, D.D. Gu, Int. J. Mach. Tools Manuf. 88 (2015) 95–107.
[14] V. Sarou-Kanian, F. Millot, J.C. Rifflet, Int. J. Thermophys. 24 (2003) 277–286.
[15] H.G. Fan, R. Kovacevic, J. Phys. D: Appl. Phys. 32 (1999) 2902–2909.
[16] W.E. King, H.D. Barth, V.M. Castillo, G.F. Gallegos, J.W. Gibbs, D.E. Hahn, C. Kamath, A.M. Rubenchik, J. Mater. Process. Technol. 214 (2014) 2915–2925.
[17] J.H. Cho, S.J. Na, J. Phys. D: Appl. Phys. 39 (2006) 5372–5378.
[18] E. Siewert, J. Schein, G. Forster, J. Phys. D: Appl. Phys. 46 (2013) 224008.
[19] S. Hardt, Phys. Fluids 17 (2005) 100601.
[20] R.P. Wang, Y.P. Lei, Y.W. Shi, Opt. Laser Technol. 43 (2011) 870–873.
[21] K. Dai, L. Shaw, Acta Mater. 52 (2004) 69–80.
[22] S.Y. Pang, L.L. Chen, J.X. Zhou, Y.J. Yin, T. Chen, J. Phys. D: Appl. Phys. 44 (2011) 025301.
[23] N.A. Vasantgadkar, U.V. Bhandarkar, S.S. Joshi, Thin Solid Films 519 (2010) 1421–1430.
[24] J.H. Cho, D.F. Farson, J.O. Milewski, K.J. Hollis, J. Phys. D: Appl. Phys. 42 (2009) 175502.